

Degradation of NiMo Catalyst Under Intermittent Operation of Anion Exchange Membrane Water Electrolyzer and its Mitigation by Carbon Encapsulation

*Sun Seo Jeon, Yunji Choi, Jae Won Lee, Robert Haaring, Wonjae Lee, Hyesoeng Jeon, Jeonghyun Nam, Eunchong Lee, Seungwoo Lee, Minjoon Kim, Yeon Sik Jung, Yousung Jung, Yun Jeong Hwang, and Hyunjoo Lee**

Developing durable platinum group metal (PGM)-free catalysts is critical for enabling cost-effective hydrogen production through anion exchange membrane water electrolyzers (AEMWEs). Here, this study presents NiMo catalysts encapsulated within defective carbon shells. Whereas conventional NiMo catalysts degrade rapidly under intermittent conditions with voltage changes, the carbon-encapsulated NiMo catalysts exhibit remarkable resistance to degradation with good hydrogen evolution reaction (HER) activity, effectively addressing the challenges associated with renewable energy integration. The carbon shells prevent oxidation-induced deactivation by inhibiting the structural transformation of metallic Ni into hydroxides accompanying volumetric expansion under open circuit voltage conditions. Using a reference electrode-integrated AEMWE, overpotential contributions are decoupled and demonstrated that the stability of HER catalyst is decisive for the durable AEMWE operation under intermittent scenarios. This study establishes a strategy for durable PGM-free catalyst development for sustainable and scalable hydrogen production.

address supply-demand mismatches.^[2] As a solution, water electrolysis powered by surplus renewable electricity has emerged as a key technology for green hydrogen production.^[3]

Among various electrolysis technologies, anion exchange membrane water electrolyzers (AEMWEs) uniquely combine the advantages of alkaline water electrolyzers (AWEs) and proton exchange membrane water electrolyzers (PEMWEs).^[4] AEMWEs utilize earth-abundant, low-cost transition metals like Ni while achieving high energy efficiencies and hydrogen purity through a membrane-electrode-assembly (MEA) design.^[5] Despite these merits, the absence of standardized MEA components, including membranes, ionomers, and catalysts, limits the scalability of AEMWEs.^[6,7]

Catalyst development continues to be a significant bottleneck, particularly for the hydrogen evolution reaction (HER) at the cathode.^[8,9] While Ni(Fe) oxide/hydroxide catalysts excel at the oxygen evolution reaction (OER) on the anode, the development of platinum group metal (PGM)-free alternatives to Pt/C for HER remains challenging.^[10–12] Recent advances have highlighted the potential of Ni-based alloys, particularly NiMo, as high-performance PGM-free HER catalysts in AEMWE.^[12–21] However, most studies focus

1. Introduction

The ongoing climate crisis necessitates a global shift toward carbon-neutral energy systems, with renewable sources such as solar and wind power leading this transition.^[1] Despite their promise, the intermittent nature of these sources necessitates reliable energy storage and carrier solutions, such as hydrogen, to

S. S. Jeon, Y. Choi, J. W. Lee, R. Haaring, W. Lee, H. Jeon, J. Nam, H. Lee
Department of Chemical and Biomolecular Engineering
Korea Advanced Institute of Science and Technology
Daejeon 34141, Republic of Korea
E-mail: azhyun@kaist.ac.kr

 The ORCID identification number(s) for the author(s) of this article can be found under <https://doi.org/10.1002/aenm.202501800>
© 2025 The Author(s). Advanced Energy Materials published by Wiley-VCH GmbH. This is an open access article under the terms of the Creative Commons Attribution-NonCommercial-NoDerivs License, which permits use and distribution in any medium, provided the original work is properly cited, the use is non-commercial and no modifications or adaptations are made.

DOI: [10.1002/aenm.202501800](https://doi.org/10.1002/aenm.202501800)

M. Kim, Y. S. Jung
Department of Materials Science and Engineering
Korea Advanced Institute of Science and Technology
Daejeon 34141, Republic of Korea
S. Lee, Y. Jung
Department of Chemical and Biological Engineering
Seoul National University
Seoul 08826, Republic of Korea
E. Lee, Y. J. Hwang
Department of Chemistry
College of Natural Sciences
Seoul National University
Seoul 08826, Republic of Korea

on continuous operation at high current density, overlooking the degradation under realistic intermittent conditions typical of renewable energy sources.^[12–19]

This work addresses the degradation of NiMo-based cathodes under intermittent operation. We identify that irreversible oxidation-induced Ni transformation causes degradation under open circuit voltage (OCV), and propose a facile carbon encapsulation strategy to enhance catalyst stability. By integrating a reference electrode within an AEMWE, we decouple overvoltage contributions and demonstrate the effectiveness of carbon-encapsulated NiMo catalysts in mitigating the degradation. This finding contributes to developing durable and cost-effective PGM-free catalysts for sustainable hydrogen production.

2. Results and Discussion

2.1. Carbon-Encapsulated NiMo Alloys

Ni₃Mo alloys were synthesized using a co-precipitation method with slight modifications to our previous work (detailed in experimental section).^[20] To encapsulate the Ni₃Mo alloy with carbon, CO gas was introduced directly after the reduction process in a tube furnace at 330 °C. The disproportionation of CO, known as the Boudouard reaction, produced elemental carbon, which deposited as thin shells around the Ni₃Mo particles. The CO treatment time was varied from 10 to 300 min, as denoted in the catalyst names (e.g., Ni₃Mo@C₆₀ indicates 60 min of CO treatment).

Transmission electron microscopy (TEM) confirmed that the average size of the particles only slightly increased from 16.6 nm in bare Ni₃Mo to 21.2 nm in Ni₃Mo@C₃₀₀ even after reductive CO treatment for 300 min, indicating that the carbon shells prevent aggregation of the particles (Figure S1, Supporting Information). The formation of carbon shell became evident as the CO treatment time increased; while Ni₃Mo@C₁₀ showed very thin carbon shells, Ni₃Mo@C₆₀ presented much thicker shells (Figure 1a–c; Figure S2, Supporting Information). Inductively coupled plasma mass spectrometry (ICP-MS) and energy-dispersive X-ray spectroscopy (EDS) analysis showed a consistent Ni:Mo molar ratio of ≈3:1 across all catalysts, matching the initial precursor composition (Table S1, Supporting Information). X-ray diffraction (XRD) patterns revealed metallic Ni peaks with slight downshifts, attributed to alloying with Mo (Figure 1d).

Temperature-programmed oxidation (TPO) analysis quantified the carbon content of the Ni₃Mo@C_x catalysts, which increased from 0.026 up to 0.173 mg_{carbon}/mg_{catalyst} with extended CO treatment times (Figure 1e). All catalysts exhibited an increase in CO₂ signals in two temperature regions: 300–500 °C (defective carbon signal) and 500–700 °C (graphitic carbon signal), with both signal intensities correlating with the duration of CO treatment (Figure S3 and Table S2, Supporting Information). This behavior indicates that prolonged CO exposure leads to thicker multi-layer carbon shells while maintaining their inherent defective characteristics. Raman spectroscopy further supported this observation, showing consistent I_D/I_G ratios across all samples, signifying that the defective nature of the carbon shells remained unchanged despite the increased thickness (Figure 1f; Table S3, Supporting Information).

The carbon encapsulation effectively protected the metallic alloy cores from air-induced oxidation. X-ray photoelectron spec-

troscopy (XPS) analysis of Ni 2p and Mo 3d spectra revealed that Ni₃Mo displayed substantial contributions from oxidized species (Ni²⁺/Ni³⁺ and Mo⁶⁺), whereas Ni₃Mo@C_x catalysts with carbon shells predominantly retained their metallic state, with minimal oxidic contributions (Figure 1g,h). Furthermore, Ni₃Mo@C_x catalysts with longer CO treatment time exhibited smaller signals typically associated with metal oxide lattice oxygen in the O 1s XPS spectra (Figure 1i). Importantly, the degree of oxidation at surface of alloy core correlated inversely with the CO treatment time. Further evidence of the metallic nature was provided by X-ray absorption near-edge structure (XANES) spectra at the Ni and Mo K-edges. Ni₃Mo exhibited the highest white line intensity for Ni K-edge, indicative of oxidized species, while longer CO treatment time reduced these features and downshifted the Mo K-edge position, signaling enhanced metallic nature (Figure S4, Supporting Information).^[22,23]

The prolonged CO treatment led to minor dealloying. Excessive carbon encapsulation resulted in expulsion of Mo from the alloy core, as evidenced by shifts to higher XRD peak positions for Ni(111), resulting in partial dealloying (Figure S5, Supporting Information). Analysis using Vegard's law estimated that the alloy core composition changed from Ni₃Mo_{1.25} in Ni₃Mo@C₁₀ to Ni₃Mo_{0.80} in Ni₃Mo@C₆₀ to Ni₃Mo_{0.42} in Ni₃Mo@C₃₀₀, whereas bare Ni₃Mo showed larger dealloying with a composition of Ni₃Mo_{0.28} due to native oxide formation (Table S4, Supporting Information). Ni₃Mo@C_x catalysts with longer CO treatment showed reduced Ni-Ni radial distances, compared to Ni₃Mo@C₁₀, in k₃-weighted Ni K-edge extended X-ray absorption fine structure (EXAFS) spectra, additionally indicating partial dealloying (Figure S6, Supporting Information). Evolution of small peaks in XRD at 37.4° and 61.6° for Ni₃Mo@C_x catalysts also indicates the formation of Mo carbide (α -MoC_x) or Mo oxy-carbide (MoOC) in the carbon shells (Figure 1d).^[24,25]

Overall, the controlled CO treatment produced Ni₃Mo@C_x catalysts with varying carbon shell amount. The degree of defective nature of the carbon layers remained unchanged regardless of their amount. The encapsulating carbon shells preserved the metallic nature of the alloy cores by preventing air-induced oxidation.

2.2. Electrochemical HER Activity and Stability of Ni₃Mo@C_x in an Alkaline Medium

The electrochemical HER activity of Ni₃Mo@C_x catalysts was evaluated in an Ar-purged 1 M KOH electrolyte using a three-electrode setup. The 1 M KOH solution was purified according to the procedure suggested previously to eliminate trace Fe species that may affect the electrochemical signals from the catalysts.^[26] Initial linear sweep voltammetry (LSV) results showed that Ni₃Mo exhibited higher HER activity compared to Ni₃Mo@C_x catalysts (Figure 2a). The onset overpotential increased as the CO treatment time increased, likely caused by the lengthened diffusion path of reactants through the porous carbon shells. The real active sites of NiMo alloys remain unclear, and recent studies showed the dynamic dissolution and re-adsorption of Mo species on Ni substrates as the origin of their high HER activity.^[27–30] Although partial dealloying might change the surface composition, the total amount of Mo species participating

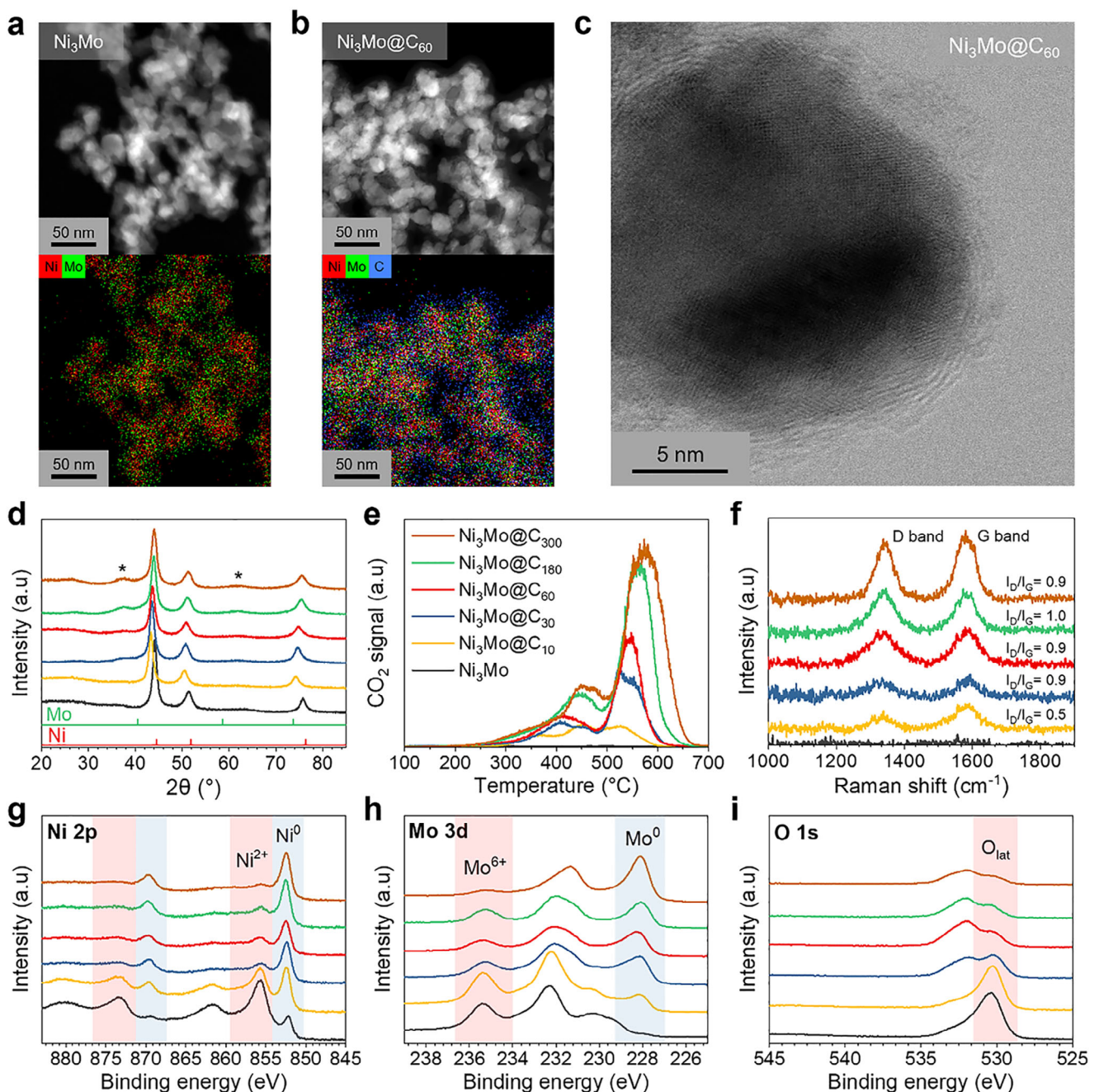


Figure 1. Structural characterization of Ni_3Mo and $\text{Ni}_3\text{Mo}@C_x$ catalysts. TEM and EDS mapping images of (a) Ni_3Mo and (b) $\text{Ni}_3\text{Mo}@C_{60}$. (c) Cs-corrected high-resolution TEM image of $\text{Ni}_3\text{Mo}@C_{60}$. (d) XRD patterns. Asterisks in XRD represent Mo carbide/oxy carbide species. e) TPO analysis, and (f) Raman spectra of carbon shells. XPS spectra at (g) Ni 2p, h) Mo 3d, and (i) O 1s regions. Red region indicates oxidized species and blue region indicate metallic species.

in the reaction was the same for all the catalysts. CO poisoning experiments further confirmed that the metal alloy cores, not the carbon layers, provide active sites (Figure S7, Supporting Information). When the metal alloy cores were leached by stirring the catalyst in nitric acid at 60 °C for 12 h, the carbon shells were only left together with residual Mo species (Figure S8, Supporting Information). The etched catalysts did not show HER activity in 1 M KOH, also indicating that the metal alloy

cores serve as primary HER-active sites (Figure S9, Supporting Information).

Stability under intermittent operation, involving exposure to open circuit voltage (OCV), is critical for water electrolysis catalysts in practical applications. To evaluate this, $\text{Ni}_3\text{Mo}@C_x$ catalysts were tested after aging for 1 h in 1 M KOH under open circuit. Ni_3Mo exhibited significant degradation, losing nearly all HER activity, while $\text{Ni}_3\text{Mo}@C_x$ catalysts showed excellent

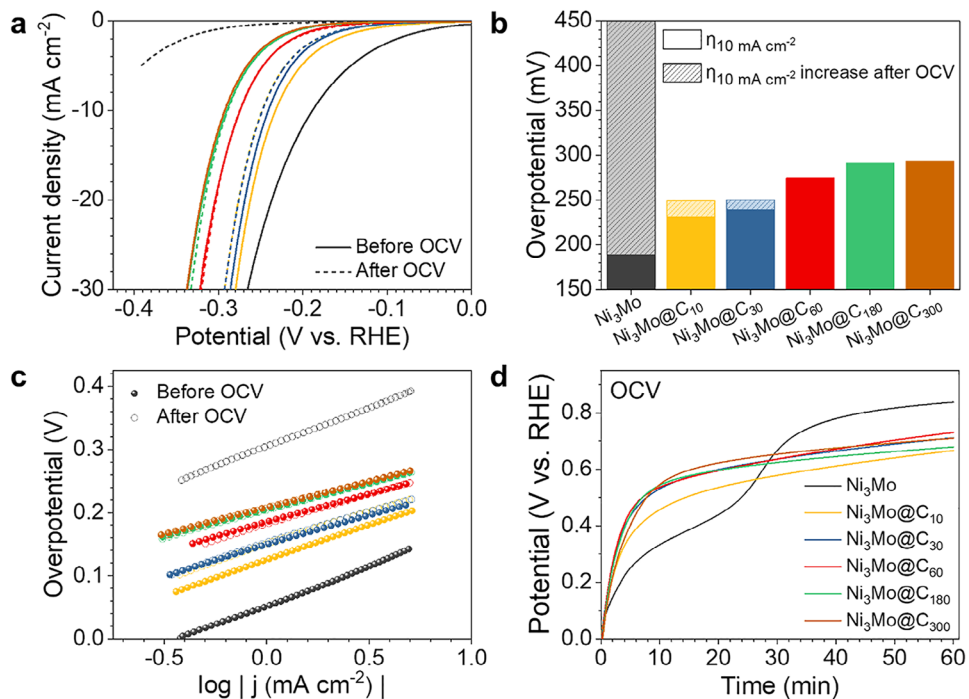


Figure 2. HER activity and stability of Ni₃Mo and Ni₃Mo@C_x catalysts before and after imposing the open circuit voltage (OCV) for 1 h in 1 M KOH. The changes in the (a) linear sweep voltammetry (LSV), b) overpotentials at -10 mA cm^{-2} , and (c) Tafel slope of Ni₃Mo and Ni₃Mo@C_x catalysts obtained before and after the aging. d) The changes in the potential upon imposing the OCV for 1 h.

retention, with thicker carbon shells (e.g., Ni₃Mo@C₆₀, Ni₃Mo@C₁₈₀, and Ni₃Mo@C₃₀₀) maintaining their initial activity completely (Figure 2a; Figure S10, Supporting Information). The overpotential at -10 mA cm^{-2} for Ni₃Mo increased from 189.1 to 450.0 mV after exposure to open circuit (Figure 2b). In contrast, catalyst with thicker carbon shells (Ni₃Mo@C₆₀, Ni₃Mo@C₁₈₀, and Ni₃Mo@C₃₀₀) showed negligible changes in overpotential, indicating superior stability. Tafel slopes also remained largely unaffected for Ni₃Mo@C_x catalysts (Figure 2c; Table S5, Supporting Information). As a catalyst with high activity and durability, Ni₃Mo@C₆₀, which showed no degradation after aging together with the lowest overpotential, was chosen and used for further characterizations and single-cell tests.

The role of carbon shells in mitigating degradation was further investigated by monitoring the potential changes during aging periods (Figure 2d). Ni₃Mo exhibited a distinct inflection in the potential, whereas Ni₃Mo@C_x catalysts did not display such behavior. The potential at the inflection point of Ni₃Mo closely aligned with the peak observed during the first anodic scan of cyclic voltammetry (Figure 3a,b; Figure S11, Supporting Information). This peak, indicated by a diamond symbol in Figure 3b and Figure S11b (Supporting Information), has been attributed to the formation of $\alpha\text{-Ni(OH)}_2$ in previous studies.^[31]

Specifically, the cyclic voltammogram (CV) can be divided into six regions, each representing a potential range for a specific stage of Ni phase transformation (Figure 3b). In stage I, immediately after HER, the catalysts maintain their metallic nature and HER activity. In stage II, the transformation from metallic phase to $\alpha\text{-Ni(OH)}_2$ phase occurs spontaneously in 1 M KOH under OCV with slow kinetics in the order of minutes to hours. This

process can be accelerated by applied potential. In stage III, $\alpha\text{-Ni(OH)}_2$ phase irreversibly transforms to $\beta\text{-Ni(OH)}_2$ phase even without applying an external potential.^[32–34] Additional anodic sweeps to higher potentials lead to further oxidation and deprotonation, forming $\beta\text{-NiOOH}$ in stage IV, which subsequently transforms into the oxygen evolution reaction (OER)-active $\gamma\text{-NiOOH}$ in stage V.^[35]

During the first cathodic scan back from 1.55 V_{RHE} to 0 V_{RHE}, the reversible transformation from $\gamma/\beta\text{-NiOOH}$ to $\beta\text{-Ni(OH)}_2$ is observed at $\approx 1.35 \text{ V}_{\text{RHE}}$ (stage III'). Here (stage III'), no indication of return to $\alpha\text{-Ni(OH)}_2$ or metallic Ni phase by reduction is observed. The absence of an anodic peak in subsequent anodic scan confirms the irreversibility of the $\beta\text{-Ni(OH)}_2$ phase transformation to $\alpha\text{-Ni(OH)}_2$ or metallic Ni (Figure S12, Supporting Information). The spontaneous transformation of Ni₃Mo from metallic phase to $\alpha\text{-Ni(OH)}_2$ phase, which readily and irreversibly converts to $\beta\text{-Ni(OH)}_2$ phase upon aging, dominantly causes the loss of HER activity in KOH electrolyte. These processes are summarized in a schematic, which is an expanded version of the original Bode cycle (Figure 3c).^[32]

The phase transformation of Ni₃Mo in 1 M KOH upon potential changes was also monitored using in situ Raman spectroscopy (Figure S13, Supporting Information). The peak arising from Ni(OH)₂ was observed upon submerging the working electrode in 1 M KOH and applying 0 V_{RHE}, indicating rapid formation of Ni hydroxide at the surface. When the potential was raised to 1.45 V_{RHE}, two peaks appeared at 474 cm⁻¹ and 556 cm⁻¹, which correspond E_g bending vibration mode and A_{1g} stretching vibration mode of Ni^{III}-O of NiOOH, respectively, indicating phase transformation to Ni oxyhydroxide.^[36] A broad peak ≈ 1050

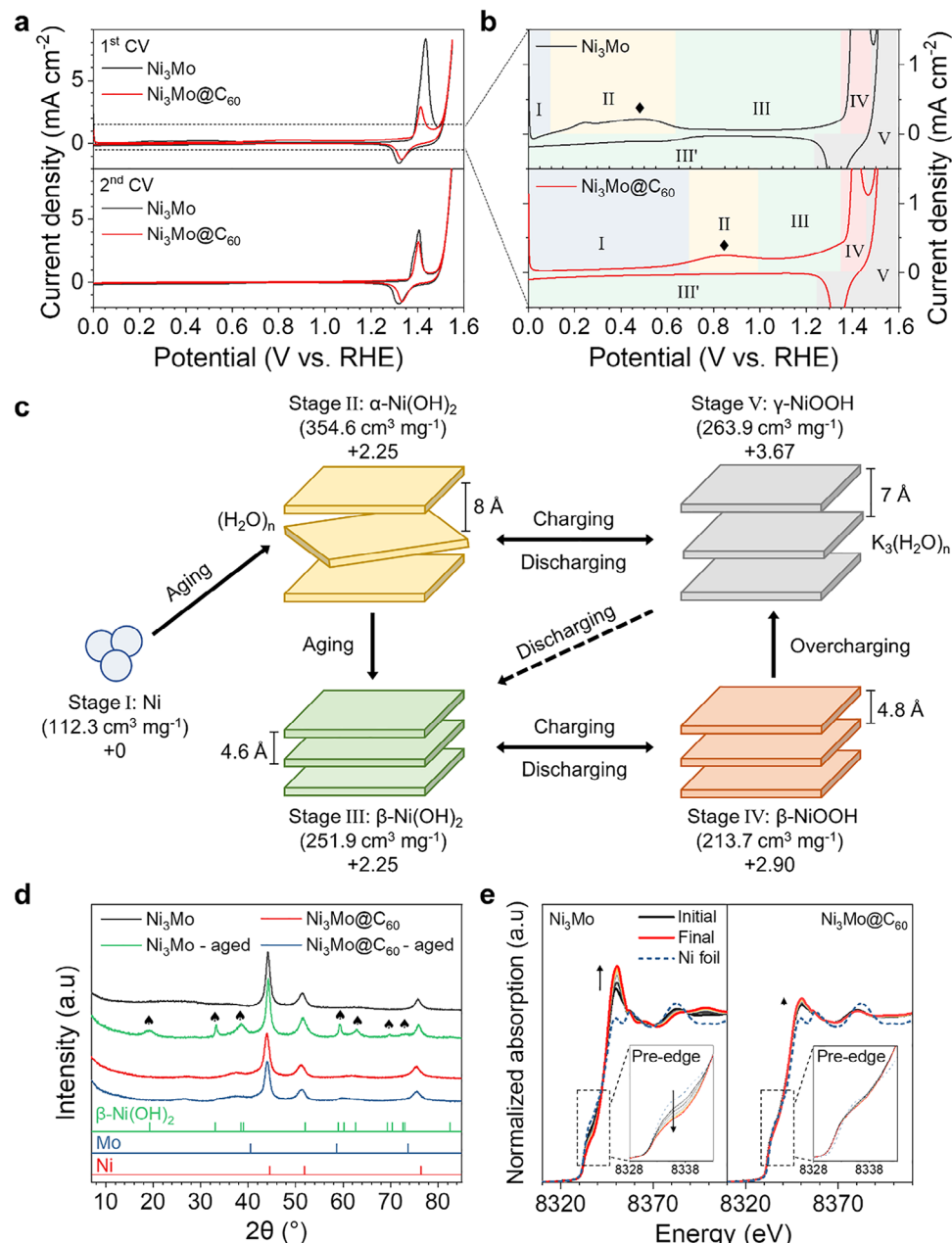


Figure 3. Phase transformation of Ni₃Mo and suppression of oxidation in Ni₃Mo@C_x catalysts in 1 M KOH. a) Cyclic voltammetry (CV) of Ni₃Mo and Ni₃Mo@C_x catalysts illustrating phase transitions from metallic Ni to hydroxides. b) Enlarged view of the first CV. The colored regions with Roman numerals indicate different potential windows of phase transitions. Diamond symbols indicate peak potentials for transformation to $\alpha\text{-Ni(OH)}_2$. c) Schematic representation of reversible and irreversible phase transitions of Ni, expanded from the original Bode's cycle, with specific volume and average oxidation states indicated. The color of diagrams corresponds with the regions of phase transition. d) XRD patterns of Ni₃Mo and Ni₃Mo@C₆₀ catalysts after aging for 24 h in 1 M KOH. Spade symbols indicate evolution of peaks corresponding to $\beta\text{-Ni(OH)}_2$. e) Operando Ni K-edge XANES spectra for Ni₃Mo and Ni₃Mo@C₆₀ catalysts obtained under OCV.

cm⁻¹ confirmed formation of OER-active $\gamma\text{-NiOOH}$.^[37] When the potential was lowered from 1.45 V_{RHE}, Ni(OH)₂ peak appeared again. Interestingly, two peaks of NiOOH subsisted down to 1.1 V_{RHE}, possibly indicating that the reductive transformation back to Ni hydroxide may not be immediate. The two peaks of NiOOH eventually disappeared when the potentials were lowered beyond 1.05 V_{RHE}, completely returning to Ni(OH)₂. Overall, the in situ

Raman spectroscopy of Ni₃Mo aligns well with potential regions of the suggested stages of phase transformation in Figure 3b.

For Ni₃Mo@C_x catalysts, the potential required for the transformation from metallic Ni to $\alpha\text{-Ni(OH)}_2$ shifted to higher values with increase in CO treatment time. (Figure S11b, Supporting Information) The peak position of phase transformation shifted from 0.75 V_{RHE} for Ni₃Mo@C₁₀ to 0.92 V_{RHE} for Ni₃Mo@C₃₀₀,

indicating that the carbon shells impeded the oxidative transformation, requiring excess overpotential for oxidation to occur. This shift expanded the potential window for metallic phase (stage I), allowing $\text{Ni}_3\text{Mo}@\text{C}_x$ catalysts to retain their metallic nature and HER activity even after 1 h of aging under open circuit in 1 M KOH (Figure 2a).

The HER activity loss upon transformation to hydroxide and the role of carbon shell in activity retention have been confirmed by exposing Ni_3Mo and $\text{Ni}_3\text{Mo}@\text{C}_{60}$ catalysts to their respective stages of transformation with varying ranges of CV (Figure S14, Supporting Information). Both catalysts showed no apparent degradation up to 0.05 V_{RHE} (stage I), while substantial loss in activity for Ni_3Mo was observed when cycled up to 0.55 V_{RHE} (stage II, beyond hydroxide formation peak) and a complete loss in activity when cycled up to 1.05 V_{RHE} (stage III) or 1.55 V_{RHE} (stage V). On the other hand, $\text{Ni}_3\text{Mo}@\text{C}_{60}$ showed no loss in activity when cycled up to 0.55 V_{RHE} (stage I), with a minor loss in activity when cycled up to 1.05 V_{RHE} (stage III, beyond hydroxide formation peak), and only a moderate loss in activity even when cycled up to 1.55 V_{RHE} (stage V).

The structural transformations between various Ni phases are accompanied by substantial volumetric changes (Figure 3c). Metallic Ni has a specific volume of 112.3 cm³ mg⁻¹, whereas $\alpha\text{-Ni(OH)}_2$ has a much higher specific volume of 354.6 cm³ mg⁻¹. The transformation of metallic Ni_3Mo to its hydroxide phase requires a significant volumetric expansion. On the other hand, the carbon shells of $\text{Ni}_3\text{Mo}@\text{C}_x$ catalysts sterically suppresses this volumetric expansion, preventing the oxidative transformation from metal to hydroxide. While the defective carbon shells permit diffusion of water molecules and hydroxide anions for HER, the carbon shells prevent the incorporation of hydroxide ions into the metal lattice for transformation to hydroxide phase. This claim is supported by the unchanging XRD patterns of $\text{Ni}_3\text{Mo}@\text{C}_{60}$ after aging in 1 M KOH, whereas Ni_3Mo developed diffraction patterns corresponding to $\beta\text{-Ni(OH)}_2$ (Figure 3d). TEM images of the aged Ni_3Mo revealed large plates, but the aged $\text{Ni}_3\text{Mo}@\text{C}_{60}$ showed no significant morphological changes (Figure S15, Supporting Information). While ICP-MS and EDS mapping revealed Mo loss for both catalysts obtained after filtration, the loss was more pronounced for Ni_3Mo (Table S6, Supporting Information).

The extent of phase transformation at the surface was investigated further by analyzing Ni 2p XPS spectra of Ni_3Mo and $\text{Ni}_3\text{Mo}@\text{C}_{60}$ after aging in 1 M KOH (Figure S16, Supporting Information). Substantial surface oxidation was observed for both catalysts, with only 2.3% zero-valent Ni (Ni^0) remaining in Ni_3Mo and 7.2% in $\text{Ni}_3\text{Mo}@\text{C}_{60}$. In order to investigate the difference in the degree of oxidation, Ni 2p XPS was re-measured after Ar⁺ sputtering for 1 min. The Ni_3Mo showed 28.2% of Ni^0 while $\text{Ni}_3\text{Mo}@\text{C}_{60}$ presented 66.0% of Ni^0 . The XPS results show that the surface oxidation was significantly suppressed with carbon shell encapsulation in $\text{Ni}_3\text{Mo}@\text{C}_x$, limiting it to the outermost surface.

For electrochemical oxidation of metallic Ni to $\alpha\text{-Ni(OH)}_2$ (transition of stage I/II) to take place, OH⁻ ion must diffuse through the defective carbon shell and be adsorbed at the Ni metal surface. The OH adsorption energy was calculated by density functional theory (DFT) to be -4.01 eV on Ni_3Mo and -2.02 eV on $\text{Ni}_3\text{Mo}@\text{C}_x$, respectively (Figure S17, Supporting Information). More negative binding energy corresponds to a

stronger bonding between OH and the catalyst surface. The carbon shells mitigate the susceptibility of surface Ni to be oxidized. Temperature-programmed desorption (TPD) and Fourier-transform infrared spectroscopy (FT-IR) measurements were performed to investigate the formation of hydroxide species on the surface of Ni_3Mo and $\text{Ni}_3\text{Mo}@\text{C}_{60}$ when they were aged in 1 M KOH for 24 h (Figure S18, Supporting Information). While the aged Ni_3Mo presented sharp peaks corresponding to the surface hydroxide species, the aged $\text{Ni}_3\text{Mo}@\text{C}_{60}$ barely showed such peaks, indicating that carbon shells surely inhibit hydroxide formation.

To monitor the transformation process, operando Ni K-edge XANES was performed for Ni_3Mo and $\text{Ni}_3\text{Mo}@\text{C}_{60}$ in 1 M KOH under OCV using a lab-made flow cell (Figure 3e; Figure S19, Supporting Information). The white line intensity of Ni_3Mo increased significantly with repeated scans, indicating Ni oxidation.^[22] The changes in the K pre-edge feature, which is associated with local coordination symmetry of Ni centres, indicated Ni-O bond formation to confirm the oxidative transformation to $\alpha/\beta\text{-Ni(OH)}_2$ under open circuit.^[38] Additionally, the changes in the post-edge oscillations, reflective of geometric rearrangements around Ni atoms, provided further evidence of transformation.^[39] $\text{Ni}_3\text{Mo}@\text{C}_{60}$, however, showed minimal changes in these features, indicating that the carbon shells effectively suppressed phase transformations and maintained initial metallic nature under open circuit in 1 M KOH (Figure 3e).

Collectively, electrochemical, ex-situ, computational, and operando structural analyses demonstrate that the carbon shells of $\text{Ni}_3\text{Mo}@\text{C}_x$ catalysts prevent oxidation of metallic core by suppressing volumetric metal lattice expansion in alkaline medium. This allows the catalysts to maintain HER activity by stabilizing the HER-active metallic phase while suppressing the formation of HER-inactive $\beta\text{-Ni(OH)}_2$ in 1 M KOH.

2.3. AEMWE Integrated with a Reference Electrode

While half-cell electrochemical analysis provides valuable insights into catalyst activity and deactivation mechanisms, it often falls short in predicting their performance in a water electrolyzer under practical operational conditions.^[40–42] Consequently, it is crucial to evaluate catalyst activity and durability within a membrane-electrode-assembly (MEA) to reflect realistic scenarios. Conventional MEAs, however, feature two coupled polarizable electrodes (cathode and anode), complicating the reliable evaluation of individual HER or OER catalysts. To address this challenge, various studies have proposed by integrating non-polarizable reference electrodes into MEAs.^[43–52] However, prior designs, especially those for AEMWE, have encountered limitations, including disconnection of the sensing electrode, potential drift, and unreliable reference potential values at high current densities, which restricted their applicability to specific conditions.^[43,48] Likely due to these challenges, to the best of our knowledge, no prior studies have demonstrated continuous monitoring of individual anode and cathode potentials over durability test in AEMWEs using an integrated reference electrode.

To leverage the advantages of a stable non-polarizable reference point, an AEMWE integrated with a reference electrode was developed (Figure S20, Supporting Information). This design,

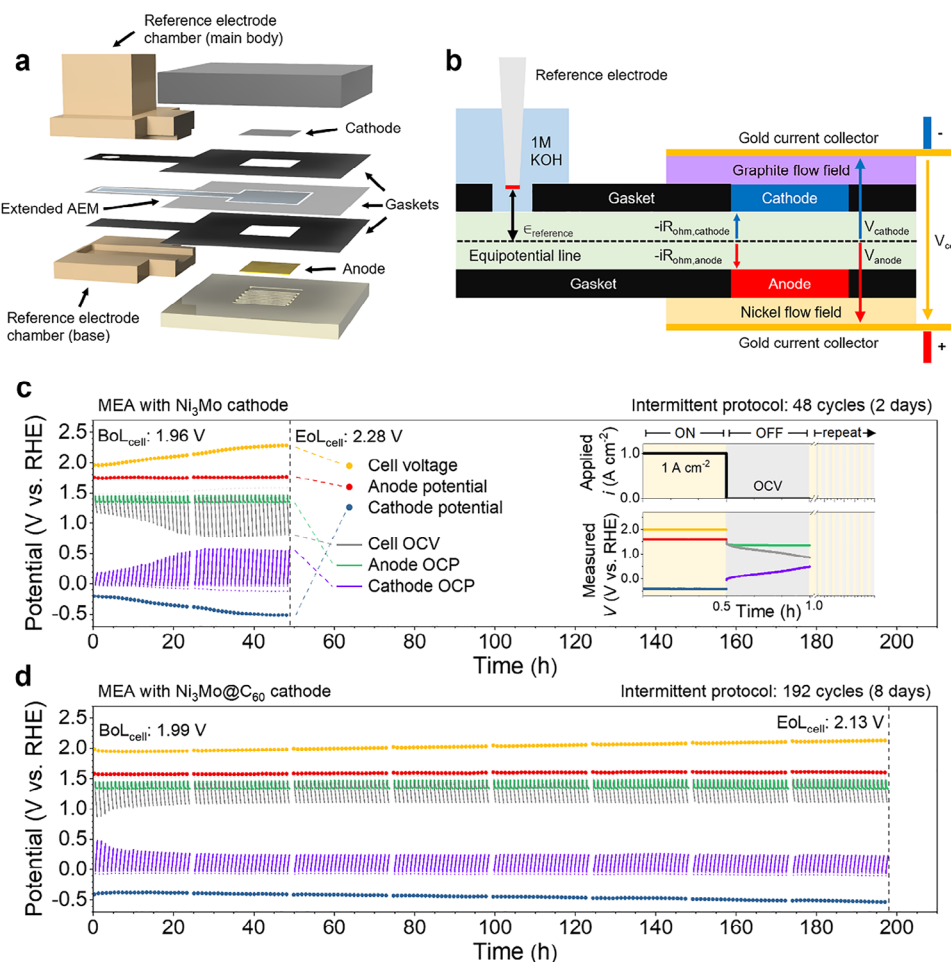


Figure 4. AEMWE integrated with a reference electrode and MEA performance with Ni_3Mo and $\text{Ni}_3\text{Mo}@C_60$ cathode catalysts under intermittent protocol. a) Exploded view of AEMWE integrated with a reference electrode. b) Schematics showing the working principle behind sensing of the electric field between the cathode and anode by the reference electrode. Cell voltage and electrode potentials at 1 A cm^{-2} and under open circuit during intermittent protocol using (c) Ni_3Mo and (d) $\text{Ni}_3\text{Mo}@C_60$. Inset figure in (c) indicates intermittent protocol used to test MEAs, consisting of repeated cycles of 30 min of chronopotentiometry at 1 A cm^{-2} and 30 min of OCV.

inspired by Boettcher et al.,^[43] uses an extended anion exchange membrane to ionically connect the MEA to an external reference electrode chamber. The MEA preparation involved precise design elements, including a custom-shaped membrane and additional gaskets to eliminate potential electrolyte leakage, ensuring stable connectivity over hundreds of hours (Figure 4a). The external chamber housed a reversible hydrogen electrode (Hydroflex, Gaskatel) immersed in 1 M KOH, connected ionically to the MEA through the extended membrane region, which functioned as a Luggin capillary to sense the electric field between planar electrodes (Figure 4b).

Additionally, instead of using a thin membrane (10–20 μm) and high operating temperatures ($\approx 80^\circ\text{C}$) to achieve high initial current densities, a moderately thick membrane (60 μm) and a moderate operating temperature (50°C) were chosen. This approach ensured sufficient membrane and ionomer stability, enabling reliable evaluation focusing on catalyst stability across various operating protocols.^[53]

Using this setup, Ni_3Mo or $\text{Ni}_3\text{Mo}@C_60$ cathode catalysts and NiFe layered double hydroxides (LDH) anode catalyst were evalu-

ated individually by decoupling electrochemical signals in MEAs under continuous and intermittent durability protocols. The continuous protocol consisted of chronopotentiometry at 1 A cm^{-2} for 24 h. Under this protocol, minimal degradation was observed for MEA with Ni_3Mo , with the cell voltages increasing only slightly from 1.98 V at the beginning of life (BoL) to 2.01 V at the end of life (EoL) (Figure S21, Supporting Information). Decoupled electrode potentials confirmed stable anode performance and only minor cathode degradation, indicating that the catalysts are robust under steady operation.

The intermittent protocol involved alternating 30 min of operation at 1 A cm^{-2} with 30 min of rest at OCV, repeated up to 192 cycles (8 days). Under this protocol, MEAs with Ni_3Mo cathodes exhibited significant degradation, as cell voltages increased from 1.96 V at BoL to 2.28 V at EoL at 1 A cm^{-2} after 48 cycles (2 days) (Figure 4c; Figure S22a, Supporting Information). Interestingly, the anode potential remained stable during both chronoamperometry and open circuit conditions, whereas the cathode potential exhibited a marked increase. The remarkable stability of NiFe LDH as an anode catalyst under

intermittent condition is attributed to its highly reversible transformation between the OER inert α -hydroxide phase and the OER-active γ -oxyhydroxide phase.^[35] In contrast, the irreversible transformation of HER-active metallic Ni₃Mo into HER-inactive hydroxides during OCV periods, as evidenced by the continuous rise in cathode potential, was the primary source of degradation. MEA with Ni₃Mo@C₆₀ cathode exhibited remarkable durability under the same conditions (Figure 4d; Figure S22b, Supporting Information). The cell voltages increased only marginally, from 1.99 V (BoL) to 2.13 V (EoL), despite extended durability testing of 192 cycles (8 days). Notably, the potential of the Ni₃Mo@C₆₀ cathode at rest state (open circuit) quickly stabilized and remained below \approx 0.3 V_{RHE}, well below the potential region associated with hydroxide formation.

The cathode layer was observed by SEM after the durability test under intermittent condition (Figure S23, Supporting Information). While the EoL Ni₃Mo cathode showed extensive β -Ni(OH)₂ formation, such transformation was absent for Ni₃Mo@C₆₀, confirming that the carbon layer effectively suppressed the hydroxide formation. Their nanoscale structure was further observed using HR-TEM and STEM. While most Ni₃Mo exhibited the transformation into platelet-like structure after 48 cycles (Figure S24, Supporting Information), Ni₃Mo@C₆₀ retained its original particle morphology showing the presence of intact carbon shells encapsulating the metal core even after 192 cycles (Figure S25, Supporting Information). The cell operation was also monitored by electrochemical impedance spectroscopy (EIS), and it clarified that the increase in cathode charge transfer resistance was the primary degradation driver for MEA with Ni₃Mo (Figure S26a, Supporting Information). By comparison, Ni₃Mo@C₆₀ exhibited significantly lower charge transfer resistance increases, corroborating its enhanced stability (Figure S26b, Supporting Information).

The integrated reference electrode enabled a rigorous evaluation of MEA performance by decoupling the origins of overpotentials (Figure 5). I-V curves obtained during the intermittent protocols were analysed using high-frequency resistance (HFR) correction to eliminate the ohmic voltage drop (Figure 5a,b). Tafel analysis of the HFR-corrected i-V curves in the kinetic region was performed to determine the Tafel slope for each curve, allowing the calculation of kinetic overpotentials at the respective electrodes (Figure S27 and Table S7, Supporting Information). This comprehensive approach enabled decoupling into multiple overpotential components, including the thermodynamic potential for water electrolysis, ohmic overpotential from membrane resistance, and individual kinetic and mass transport overpotentials for the cathode and anode.

A detailed overpotential analysis revealed that the kinetic overpotential at the Ni₃Mo cathode increased sharply during the 2-day intermittent protocol, ultimately becoming the dominant contributor to the cell overvoltage (Figure 5c,d). In contrast, for Ni₃Mo@C₆₀, the kinetic overpotential at the cathode was initially larger than Ni₃Mo, but the overpotential only slightly increased after the 8-day intermittent protocol (Figure 5e,f). A comparison of overpotential contributions at 1 A cm⁻² for MEAs with Ni₃Mo and Ni₃Mo@C₆₀ before and after the intermittent protocol clearly illustrates the difference in degradation profiles (Figure S28, Supporting Information).

These findings highlight the critical role of carbon encapsulation in preventing irreversible catalyst deactivation of NiMo alloy under intermittent conditions of AEMWE. The incorporation of a reference electrode into the AEMWE allowed for precise decoupling of overvoltage contributions, offering valuable insights into degradation mechanisms and enabling a rigorous assessment of catalyst durability under realistic operating conditions.

3. Conclusion

This work investigated the degradation mechanisms and mitigation strategies for NiMo-based HER catalysts in AEMWEs under intermittent operating conditions. By synthesizing and characterizing carbon-encapsulated NiMo alloys (Ni₃Mo@C_x), we demonstrated that defective carbon shells preserve the metallic integrity of Ni₃Mo cores. These carbon shells effectively suppress the irreversible oxidative transformation of metallic Ni to HER-inactive hydroxide phases, driven by volumetric lattice expansion under OCV conditions in 1 M KOH electrolyte. Electrochemical evaluations under intermittent operation confirmed the stability of the carbon-encapsulated catalysts, with minimal degradation observed even after extended intermittent cycling for 8 days. Notably, the integration of a reference electrode into the AEMWE enabled the decoupling of overvoltage contributions, revealing that the degradation of NiMo cathode is the primary cause of overall cell performance decline under intermittent conditions, rather than the anode degradation. This finding highlights the critical importance of ensuring the stability of HER catalyst at the cathode to achieve stable intermittent operation of AEMWEs. Overall, this study offers a promising pathway for achieving cost-effective and durable hydrogen production using PGM-free AEMWE systems, especially under intermittent renewable energy scenarios.

4. Experimental Section

Chemicals: Nickel (II) chloride hexahydrate (NiCl₂·6H₂O, 99.999% metal basis), molybdenum chloride (MoCl₅, 95%), sodium hydroxide (NaOH, \geq 97%), sodium carbonate (Na₂CO₃, \geq 99.5%), iron chloride (FeCl₃, 97%), and Nafion perfluorinated resin solution (5 wt.% in lower aliphatic alcohols/water) were procured from Sigma-Aldrich. 2-propanol ((CH₃)₂CHOH, 99.7%) was purchased from Junsei. PiperION anion exchange membrane (PiperION-A60-HCO₃, Versogen), Toray Paper 090 carbon paper (TGP-H-090), and Nickel foam (80-120 PPI – 1 mm) were purchased from Fuel Cell Store. All chemicals were used as received without further purification. Deionized water (18.2 MΩ·cm) was used for all experiments.

Catalyst Synthesis: A homogeneous metal precursor solution was prepared by dissolving 6.417 g of NiCl₂·6H₂O and 2.459 g of MoCl₅ in 45 mL of deionized water (molar ratio of 3:1). Separately, an alkaline solution was prepared by dissolving 3.060 g of NaOH and 2.623 g of Na₂CO₃ in 45 mL of deionized water. Both solutions were added dropwise into 90 mL of deionized water under stirring, maintaining a pH of \approx 8.5. The resulting mixture was aged overnight, washed thoroughly with deionized water and ethanol, and dried at 60 °C. The obtained Ni₃Mo-hydroxide precursor powder was ground and stored in a vacuum desiccator. Approximately 330 mg of the precursor was placed in an alumina boat inside a tube furnace. The temperature was ramped to 330 °C at 10 °C min⁻¹ and held for 40 min in an atmosphere of H₂/N₂ (6.5/156 sccm). The product was then cooled to room temperature under N₂ flow, then Ni₃Mo catalyst was obtained. Carbon-encapsulated Ni₃Mo catalyst (Ni₃Mo@C_x) was synthesized by

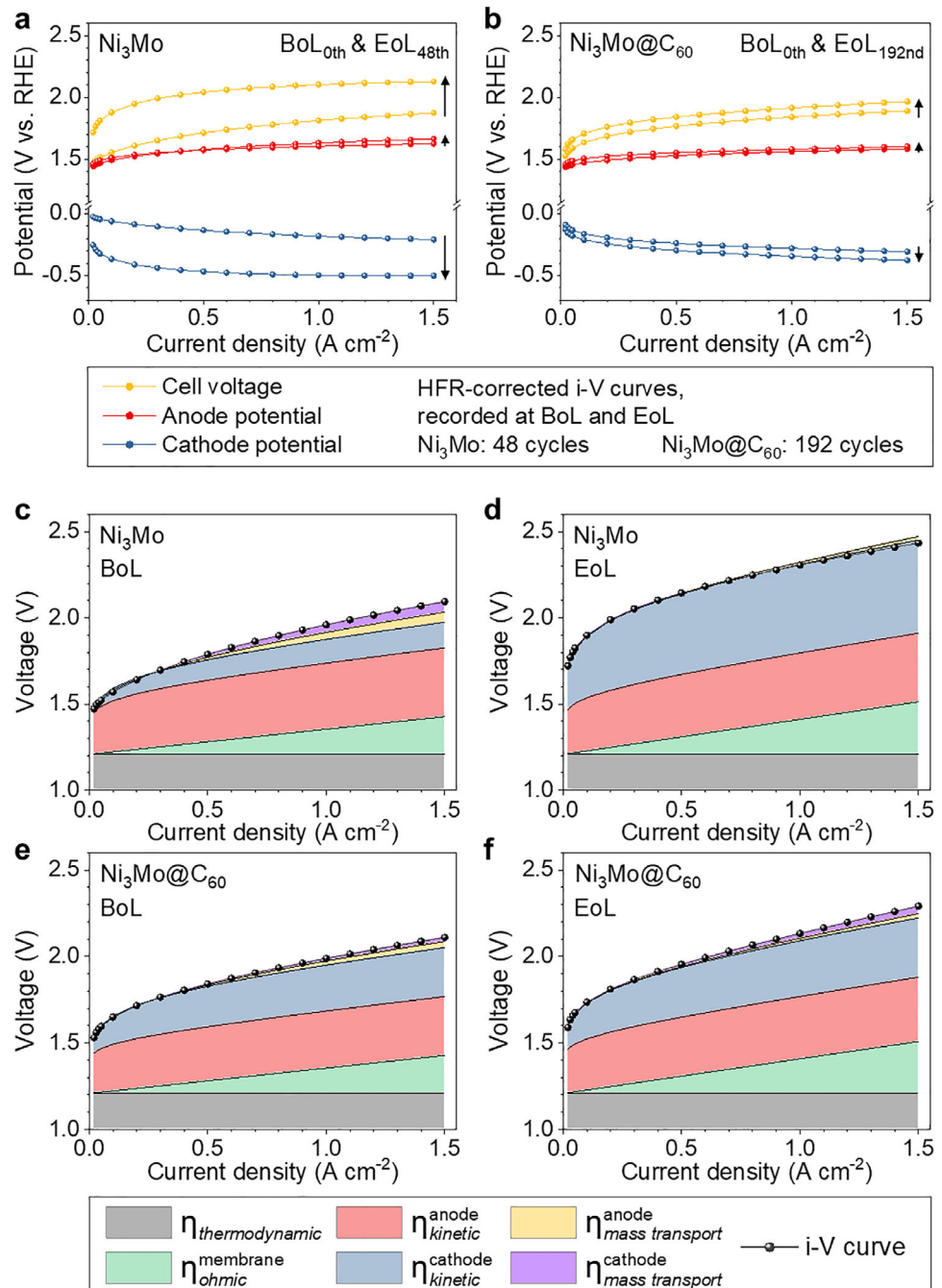


Figure 5. The beginning of life (BoL) and the end of life (EoL) i-V curves after the correction using high-frequency resistance (HFR) for MEA with (a) Ni₃Mo and (b) Ni₃Mo@C₆₀ cathode catalysts. The intermittent protocol was the same as in Figure 4. Decoupling overpotentials for the MEA with Ni₃Mo at (c) BoL and (d) EoL, and with Ni₃Mo@C₆₀ at (e) BoL and (f) EoL. EoL i-V curve was measured after 48 cycles of intermittent protocols for Ni₃Mo and after 192 cycles for Ni₃Mo@C₆₀.

introducing CO gas to the Ni₃Mo catalyst. Following the reduction, the catalyst was exposed to CO (156 sccm) at 330 °C with varying durations (10–300 min). The catalysts were then cooled to room temperature under N₂ flow. The duration of CO treatment was indicated in the catalyst name (e.g., Ni₃Mo@C₆₀ for 60 min).

NiFe LDH catalysts were synthesized as an OER catalyst, following our previous work.^[54] A metal precursor solution was prepared by dis-

solving 6.417 g of NiCl₂·6H₂O and 1.459 g of FeCl₃ in 45 mL of deionized water. An alkaline solution was prepared as described for Ni₃Mo hydroxide synthesis. Both solutions were added dropwise into 90 mL of deionized water under stirring, maintaining a pH of ≈8.5. The resulting mixture was aged overnight, washed with deionized water and ethanol, and dried at 60 °C. The dried powder was ground and used directly.

Characterizations: Transmission electron microscopy (TEM; FEI Tecnai G2 F30 S-Twin) was performed using a 300-kV electron beam. X-Ray diffractometer (XRD; SmartLab, Rigaku) was used to obtain high resolution powder X-ray diffraction patterns. The elemental contents of Ni and Mo in the catalyst were measured using inductively coupled plasma mass spectrometry (ICP-MS; Perkin Elmer NexION 1000). TPO and TPD were conducted using a BELCAT-B (MicrotracBEL) equipped with a mass spectrometer (BELMASS). 50 mg of catalyst powder was pre-treated with 50 sccm of He at 45 °C for 1 h. For TPO, the temperature was raised to 900 °C under a 5% O₂/He gas at 10 °C min⁻¹. For TPD, the temperature was ramped to 900 °C under continuous He flow at 10 °C min⁻¹. Ex-situ Raman spectra of Ni₃Mo@C_x catalyst powders were obtained using confocal Raman spectroscopy (Nanobase XperRam S) with laser wavelength of 523 nm and laser power of 9.2 mW. Microscope with 50 magnification lens and gratings of 1800 grooves per 1 mm was used. X-ray photoelectron spectroscopy (XPS; Thermo VG Scientific, K-alpha) was used for measuring the surface composition of the catalysts. Ar⁺ sputtering was carried out for 1 min with ion energy of 2 kV, with sputter raster size of 2 mm. Cluster ions (Ar⁺_n) were used to minimize surface damage. The binding energies were corrected using the maximum intensity of the reference C 1s signal at 284.8 eV. Scanning electron microscopy (SEM; Hitachi SU5000) and energy dispersive X-ray spectroscopy (EDS) was performed to observe the morphology and the electrode surface. FT-IR was conducted using a Nicolet iS-50 instrument (Thermo Scientific) with a KBr window. The catalyst was mixed with KBr powder, thoroughly ground, loaded into a sample cup, and placed in the sample cell. Prior to measurement, the sample was pre-treated at 100 °C for 1 h under an Ar atmosphere. Spectra were recorded under Ar to avoid ambient interference.

In situ Raman spectroscopy measurement was carried out using an In-Via Qontor confocal Raman microscope (RENISHAW) with 532 nm laser and a custom-made electrochemical cell through a 63x water-immersion objective lens. Exposure time was 20 s with 3 accumulation conditions. Under the three-electrode system, Ni₃Mo catalyst was spray-coated on carbon paper and used as a working electrode. The Pt wire and Hg/HgO (1 M KOH) were utilized as counter and reference electrode, respectively, in 1 M KOH. To obtain Raman spectra under steady-state conditions at various applied potentials, multi-step chronoamperometry was conducted at each potential during both the anodic sweep (0 V_{RHE} to 1.45 V_{RHE}) and the cathodic sweep (1.45 V_{RHE} to 0 V_{RHE}).

X-ray absorption spectroscopy (XAS) was performed at the 10C Wide XAFS beamline of the Pohang Light Source. The Ni and Mo K edge spectra of powder catalysts were acquired in transmission mode. The *operando* Ni K edge spectra of the catalyst layer were acquired in fluorescence mode. A lab-made flow-cell attached to a diaphragm pump (SIMDOS 02, KNF) was used to deliver 1 M KOH to the catalyst layer. Graphene sheets (Graphene Supermarket), Pt wire, and Hg/HgO electrode were used as working, counter, and reference electrodes, respectively. The catalyst loading was 0.25 mg_{metal} cm⁻². All the measurements were calibrated using a reference metal foil. The XAS data were processed with ATHENA software program to obtain XANES and k₃-weighted EXAFS spectra. All the electrochemical measurements were carried out using VSP-300 (Biologic) with additional 10 A / 5 V current booster.

Half-Cell Measurements: Half-cell electrochemical measurements were performed in a three-electrode setup with a glassy carbon rotating disk electrode (RDE, PINE) as the working electrode, a carbon rod as the counter electrode, and a reversible hydrogen electrode (RHE, Hydroflex, Gaskatel) as the reference electrode at 1600 rpm and room temperature. 1 M KOH was used as the electrolyte after being purged with Ar gas to ensure an inert atmosphere. Particularly, Fe-free 1 M KOH was prepared following the procedure reported previously,^[28] and this Fe-free electrolyte solution was used for all the measurements in this work. The catalyst ink was prepared by dispersing 5 mg of catalyst and 1.25 mg of Vulcan carbon in 2 mL of isopropanol, 0.5 mL of deionized water, and 20 μL of Nafion ionomer dispersion. After sonicating for 30 min, 9.90 μL of the ink was drop-cast onto the RDE, achieving a catalyst loading of 0.10 mg cm⁻². To prevent deactivation of Ni-based catalysts, a potential of 0 V_{RHE} was applied immediately as the working electrode was immersed in the electrolyte. Initial activity of the catalyst was obtained by LSV from 0 V_{RHE} to

–0.45 V_{RHE} at a scan rate of 10 mV s⁻¹. The potential at open circuit was measured over 60 min, then another LSV was carried out. CV was carried out from 0 V_{RHE} to 1.55 V_{RHE} for 2 cycles at scan rate of 10 mV s⁻¹ to observe for Ni phase transformation. EIS at 0 V_{RHE} was carried out after each LSV for manual *iR*-correction.

AEMWE Integrated with a Reference Electrode: AEMWE measurements were conducted using a commercial single-cell setup (Fuel Cell Technologies) integrated with a custom-designed reference electrode chamber. The cathode catalyst ink was prepared by dispersing 156.25 mg of Ni₃Mo or Ni₃Mo@C₆₀ and 39.06 mg of Vulcan carbon into a solution of 12.5 mL isopropyl alcohol, 3.125 mL deionized water, and 0.913 mL of 5 wt% PiperION ionomer. The mixture was ultrasonicated for 1 h, then spray-coated onto carbon paper placed on a hot plate heated to 80 °C. The catalyst-coated carbon paper was cut to serve as cathodes, with a target catalyst loading of 2.0 mg cm⁻². The anode catalyst ink was prepared by dispersing 156.25 mg of NiFe LDH into a solution of 12.5 mL isopropyl alcohol, 3.125 mL deionized water, and 0.913 mL of 5 wt% PiperION ionomer. This ink was also ultrasonicated for 1 h and spray-coated onto Ni foam on a hot plate heated to 80 °C. The catalyst-coated Ni foam was cut to serve as anodes, with a target catalyst loading of 2.5 mg cm⁻². Membrane electrode assembly (MEA) was fabricated on the cell hardware without hot-pressing. Three gaskets, shaped as illustrated in Figure 4a, were used to prevent electrolyte leakage. The PiperION anion exchange membrane was cut to fit the middle gasket, activated in 1 M KOH for 1 h, rinsed with deionized water, and placed between the cathode and anode on graphite and Ni blocks, each featuring a single serpentine flow pattern. The cell was assembled with a torque of 50 kgf·cm and heated to 50 °C using an integrated heating rod. The active area of the MEA was 5 cm². The reference electrode chamber was fabricated using PEEK to hold a reversible hydrogen electrode (Hydroflex, Gaskatel) immersed in 1 M KOH. Ionic connectivity between the reference electrode and the MEA was maintained using an extended section of the anion exchange membrane, as depicted in Figure 4b. Separate reservoirs containing 0.5 L of 1 M KOH were used as the catholyte and anolyte. Both electrolytes were heated to 50 °C and circulated at a flow rate of 25 mL min⁻¹ using peristaltic pumps.

Activity and Durability Testing Protocols in AEMWE: The MEA was activated using chronopotentiometry at 0.05 A cm⁻² until the performance was stabilized. Subsequently, *i*-V curves were recorded by holding each current density for 1 min, ranging from 0.02 to 1.5 A cm⁻² at specified intervals. Galvanostatic electrochemical impedance spectroscopy (GEIS) was performed at 50 mA cm⁻² from 100 kHz to 0.1 Hz with 10 mV amplitude after each *i*-V measurement to measure the high-frequency resistance (HFR). Durability was tested under two protocols. The continuous protocol involved chronopotentiometry at 1 A cm⁻² for 24 h, while the intermittent protocol consisted of repeated cycles of 30 min at 1 A cm⁻² followed by 30 min at OCV. These cycles were repeated up to 192 times (8 days, 192 h). Degradation was assessed by obtaining *i*-V curves every 24 cycles.

Density Functional Theory (DFT) Calculations: All of DFT calculations used in this study were performed by the Vienna ab initio simulation package (VASP).^[55] The projector augmented wave method (PAW) was used to represent the core-valence electron interaction.^[56] The exchange and correlation energy were calculated by revised Perdew-Burke-Ernzerhof (rPBE) functional within the generalized gradient approximation (GGA).^[57] All calculations were performed with a plane wave cutoff energy of 400 eV and a *k*-points sampling of 3 × 3 × 1 with Monkhorst-Pack scheme. The computational convergence was within 10⁻⁵ eV and 0.05 eV Å⁻¹ for energy and force, respectively. For all calculations, spin polarization effect was considered. For the interaction between graphene layers, DFT-D3 method was used for the correction of van der Waals force. A perpendicular vacuum space 15 Å was used to ensure that the system has little interaction with its images. Ni₃Mo(101) surface was modelled using a slab of a 2 × 2 unit cell with six atomic layers.^[20] To take into account of carbon shell, two graphene layers were placed on the top of Ni₃Mo(101) surface. 40 carbon atoms per layer was used in the supercell to ensure symmetry in periodic boundaries. The binding energies (*E_b*) of the hydroxyl ion and catalyst surface was calculated by a following equation: *E_b* = *E_{adsorbate/catalyst}* − *E_{adsorbate}* − *E_{catalyst}*, where *E_{adsorbate/catalyst}*, *E_{adsorbate}*, and *E_{catalyst}* correspond

to the total energy of catalyst adsorbed by chemical species on the surface, the total energy of an isolated adsorbate, and a clean catalyst, respectively. The more negative E_b corresponds to stronger bond between hydroxyl ion and the catalyst surface.

Supporting Information

Supporting Information is available from the Wiley Online Library or from the author.

Acknowledgements

This work was financially supported by the National Research Foundation of Korea (2021R1A3B1076715 and 2021M3H4A3A02086516), funded by the Ministry of Education, Science and Technology, Republic of Korea. The experiments at Pohang Light Source were supported in part by MSIP and POSTECH.

Conflict of Interest

The authors declare no conflict of interest.

Author Contributions

S.S.J. and H.L. conceived the project and wrote the manuscript. S.S.J. synthesized the catalysts, performed characterizations, designed operando XAS flow-cell and reference-electrode-integrated AEMWE, carried out electrochemical analysis. Y.C. carried out TPO, TPD, and FTIR analysis of the catalysts. J.L. helped with designing of operando XAS flow-cell and reference-electrode-integrated AEMWE. R.H. carried out SEM analysis of the electrodes. W.L., H.J., and J.N. helped with characterizations of the catalysts. M.K. and Y.S.J. carried out ex-situ Raman spectroscopy of the catalysts. E.L. and Y.J.H. carried out insitu Raman spectroscopy. S.L. and Y.J. performed DFT calculations. All authors have read and commented on the manuscript.

Data Availability Statement

The data that support the findings of this study are available from the corresponding author upon reasonable request.

Keywords

anion exchange membrane, hydrogen evolution reaction, intermittent operation, nickel, water electrolysis

Received: March 31, 2025

Revised: May 9, 2025

Published online: May 27, 2025

- [1] Q. Hassan, A. M. Abdulateef, S. A. Hafedh, A. Al-samari, J. Abdulateef, A. Z. Sarneen, H. M. Salman, A. K. Al-Jiboory, S. Wieteska, M. Jaszczer, *Int. J. Hydrogen Energy* **2023**, *48*, 17383.
- [2] H. Koijima, K. Nagasawa, N. Todoroki, Y. Ito, T. Matsui, R. Nakajima, *Int. J. Hydrogen Energy* **2023**, *48*, 4572.
- [3] S. S. Kumar, H. Lim, *Energy Rep.* **2022**, *8*, 13793.

- [4] M. F. Lagadec, A. Grimaud, *Nat. Mater.* **2020**, *19*, 1140.
- [5] S. S. Jeon, W. Lee, H. Jeon, H. Lee, *ChemSusChem* **2024**, *17*, 202301827.
- [6] N. Du, C. Roy, R. Peach, M. Turnbull, S. Thiele, C. Bock, *Chem. Rev.* **2022**, *122*, 11830.
- [7] E. K. Volk, M. E. Kreider, S. Kwon, S. M. Alia, *EES Catalysis* **2024**, *2*, 109.
- [8] A. Y. Faid, S. Sunde, *Energy Technol.* **2022**, *10*, 2200506.
- [9] S. A. Lee, J. Kim, K. C. Kwon, S. H. Park, H. W. Jang, *Carbon Neutralization* **2022**, *1*, 26.
- [10] C. Santoro, A. Lavacchi, P. Mustarelli, V. Di Noto, L. Elbaz, D. R. Dekel, F. Jaouen, *ChemSusChem* **2022**, *15*, 202200027.
- [11] M. Klingenhof, H. Trzesniowski, S. Koch, J. Zhu, Z. Zeng, L. Metzler, A. Klinger, M. Elshamy, F. Lehmann, P. W. Buchheister, A. Weisser, G. Schmid, S. Vierrath, F. Dionigi, P. Strasser, *Nat. Catal.* **2024**, *7*, 1213.
- [12] Z. Li, G. Lin, L. Wang, H. Lee, J. Du, T. Tang, G. Ding, R. Ren, W. Li, X. Cao, S. Ding, W. Ye, W. Yang, L. Sun, *Nat. Catal.* **2024**, *7*, 944.
- [13] L. Wang, T. Weissbach, R. Reissner, A. Ansar, A. S. Gago, S. Holdcroft, K. A. Friedrich, *ACS Appl. Energy Mater.* **2019**, *2*, 7903.
- [14] P. Chen, X. Hu, *Adv. Energy Mater.* **2020**, *10*, 2002285.
- [15] M. Klingenhof, S. Selve, C. M. Günther, J. Schmidt, F. Razmjooei, P. Strasser, S.-A. Ansar, *ACS Appl. Energy Mater.* **2024**, *7*, 6856.
- [16] A. Y. Faid, A. Oyarcé Barnett, F. Seland, S. Sunde, *Catalysts* **2018**, *8*, 614.
- [17] M. R. Kraglund, M. Carmo, G. Schiller, S. A. Ansar, D. Aili, E. Christensen, J. O. Jensen, *Energy Environ. Sci.* **2019**, *12*, 3313.
- [18] S. E. Jun, S.-W. Myeong, B.-G. Cho, J. Kim, S. J. Park, C. Kim, T. H. Lee, S. Lee, J. Y. Kim, M. S. Kwon, J. H. Kang, K. C. Kwon, S. M. Choi, H. W. Jang, S. H. Park, *Appl. Catal. B: Environ. Energy* **2024**, *358*, 124364.
- [19] Y. Chen, K. Yue, J.-W. Zhao, Z. Cai, X. Wang, Y. Yan, *Chem. Eng. J.* **2023**, *466*, 143097.
- [20] W. Lee, H. Yun, Y. Kim, S. S. Jeon, H. T. Chung, B. Han, H. Lee, *ACS Catal.* **2023**, *13*, 11589.
- [21] E. Schropp, A. A. García Blanco, S. Murcia-López, G. Naumann, M. Gaderer, *J. Power Sources* **2024**, *614*, 235031.
- [22] M. Wang, Z. Feng, *Curr. Opin. Electrochem.* **2021**, *30*, 100803.
- [23] T. Ressler, R. E. Jentoft, J. Wienold, M. M. Günter, O. Timpe, *J. Phys. Chem. B* **2000**, *104*, 6360.
- [24] C. Wan, Y. N. Regmi, B. M. Leonard, *Angew. Chem., Int. Ed.* **2014**, *53*, 6407.
- [25] Y. Zhou, W. Yuan, M. Li, Z. Xie, X. Song, Y. Yang, J. Wang, L. Li, W. Ding, W.-F. Lin, Z. Wei, *Nat. Energy* **2024**, *9*, 1297.
- [26] L. Trotochaud, S. L. Young, J. K. Ranney, S. W. Boettcher, *J. Am. Chem. Soc.* **2014**, *136*, 6744.
- [27] W. Du, Y. M. Shi, W. Zhou, Y. F. Yu, B. Zhang, *Angew. Chem., Int. Ed.* **2021**, *60*, 7051.
- [28] J. A. Bau, S. M. Kozlov, L. M. Azofra, S. Ould-Chikh, A.-H. Emwas, H. Idriss, L. Cavallo, K. Takanabe, *ACS Catal.* **2020**, *10*, 12858.
- [29] D. Neumüller, L. D. Rafailović, I. A. Pašti, T. Griesser, C. Gammer, J. Eckert, *Small* **2024**, *20*, 2402200.
- [30] Z. Zhang, L. Li, Y. Li, Y. Zheng, Q. Wu, L. Xie, B. Luo, J. Hao, W. Shi, *Chem. Eng. J.* **2023**, *469*, 143846.
- [31] S. L. Medway, C. A. Lucas, A. Kowal, R. J. Nichols, D. Johnson, *J. Electroanal. Chem.* **2006**, *587*, 172.
- [32] H. Bode, K. Dehmelt, J. Witte, *Electrochim. Acta* **1966**, *11*, 1079.
- [33] M. C. Bernard, P. Bernard, M. Keddam, S. Senyach, H. Takenouti, *Electrochim. Acta* **1996**, *41*, 91.
- [34] P. Oliva, J. Leonardi, J. F. Laurent, C. Delmas, J. J. Braconnier, M. Figlarz, F. Fievet, A. d. Guibert, *J. Power Sources* **1982**, *8*, 229.
- [35] F. Dionigi, Z. Zeng, I. Sinev, T. Merzdorf, S. Deshpande, M. B. Lopez, S. Kunze, I. Zegkinoglou, H. Sarodnik, D. Fan, A. Bergmann, J. Drnec, J. F. d. Araujo, M. Gliech, D. Teschner, J. Zhu, W.-X. Li, J. Greeley, B. R. Cuanya, P. Strasser, *Nat. Commun.* **2020**, *11*, 2522.

- [36] J. Choi, S. Yoo, P. M. Nguyen, E. Lee, H. Shin, Y. J. Hwang, *ACS Catal.* **2025**, *15*, 6906.
- [37] S. Lee, Y.-C. Chu, L. Bai, H. M. Chen, X. Hu, *Chem. Catalysis* **2023**, *3*, 100475.
- [38] E. I. Solomon, B. Hedman, K. O. Hodgson, A. Dey, R. K. Szilagyi, *Coord. Chem. Rev.* **2005**, *249*, 97.
- [39] D. K. Bediako, B. Lassalle-Kaiser, Y. Surendranath, J. Yano, V. K. Yachandra, D. G. Nocera, *J. Am. Chem. Soc.* **2012**, *134*, 6801.
- [40] M. Fathi Tovini, A. Hartig-Weiß, H. A. Gasteiger, H. A. El-Sayed, *J. Electrochem. Soc.* **2021**, *168*, 014512.
- [41] T. Lazaridis, B. M. Stühmeier, H. A. Gasteiger, H. A. El-Sayed, *Nat. Catal.* **2022**, *5*, 363.
- [42] A. J. Shih, M. C. O. Monteiro, F. Dattila, D. Pavesi, M. Philips, A. H. M. da Silva, R. E. Vos, K. Ojha, S. Park, O. van der Heijden, G. Marcandalli, A. Goyal, M. Villalba, X. Chen, G. T. K. K. Gunasooriya, I. McCrum, R. Mom, N. López, M. T. M. Koper, *Nat. Rev. Methods Primers* **2022**, *2*, 84.
- [43] Q. Xu, S. Z. Oener, G. Lindquist, H. Jiang, C. Li, S. W. Boettcher, *ACS Energy Lett.* **2021**, *6*, 305.
- [44] L. V. Bühre, S. Bullerdiek, P. Trinke, B. Bensmann, A.-L. E. R. Deutsch, P. Behrens, R. Hanke-Rauschenbach, *J. Electrochem. Soc.* **2022**, *169*, 124513.
- [45] E. Brightman, J. Dodwell, N. van Dijk, G. Hinds, *Electrochem. Commun.* **2015**, *52*, 1.
- [46] A. Hartig-Weiß, M. Bernt, A. Siebel, H. A. Gasteiger, *J. Electrochem. Soc.* **2021**, *168*, 114511.
- [47] A. Y. Faid, L. Xie, A. O. Barnett, F. Seland, D. Kirk, S. Sunde, *Int. J. Hydrogen Energy* **2020**, *45*, 28272.
- [48] O. Sorsa, J. Nieminen, P. Kauranen, T. Kallio, *J. Electrochem. Soc.* **2019**, *166*, F1326.
- [49] A. W. Tricker, J. K. Lee, J. R. Shin, N. Danilovic, A. Z. Weber, X. Peng, *J. Power Sources* **2023**, *567*, 232967.
- [50] P. K. Giesbrecht, M. S. Freund, *ACS Appl. Energy Mater.* **2024**, *7*, 7272.
- [51] M. Huang, K. Lao, L. Ma, J. Tao, X. Zhuang, T. Hu, Y. Pan, H. Liu, L. Wen, S. Xu, X. Liu, Y. Wu, S. Li, H. B. Tao, N. Zheng, *ACS Appl. Mater. Interfaces* **2024**, *16*, 39408.
- [52] N. Guruprasad, J. van der Schaaf, M. T. de Groot, *J. Power Sources* **2024**, *613*, 234877.
- [53] Y. Yang, P. Li, X. Zheng, W. Sun, S. X. Dou, T. Ma, H. Pan, *Chem. Soc. Rev.* **2022**, *51*, 9620.
- [54] S. S. Jeon, J. Lim, P. W. Kang, J. W. Lee, G. Kang, H. Lee, *ACS Appl. Mater. Interfaces* **2021**, *13*, 37179.
- [55] J. Hafner, *J. Comput. Chem.* **2008**, *29*, 2044.
- [56] P. E. Blochl, *Phys. Rev. B Condens. Matter.* **1994**, *50*, 17953.
- [57] B. Hammer, *Phys. Rev. B Condens. Matter.* **1999**, *59*, 7413.